

Biosensors in Silicon on Insulator.

Peter Bienstman, Katrien De Vos, Tom Claes, Peter Debackere, Roel Baets, Jordi Girones ^b
and Etienne Schacht ^b

Ghent University - Imec ^a
Department of Information Technology
Sint-Pietersnieuwstraat 41
9000 Gent, Belgium

Ghent University ^b
Polymer Material Research Group
Krijgslaan 281
9000 Gent, Belgium

ABSTRACT

We present several nanophotonic biosensors on silicon-on-insulator: ring resonator based devices, slotted ring resonators to increase the interaction between light and the sample, and finally devices based on nanoplasmonic interferometers.

Keywords: nanophotonics, biosensors, silicon-on-insulator, ring resonators, slotted waveguides, plasmonics, interferometers

1. INTRODUCTION

Silicon-on-insulator is a very attractive platform for nanophotonics sensors. Because of its low cost, it offers the potential for cheap, even disposable biosensors. Very small structures can be realised, which is advantageous for multiparameter analysis, i.e. the integration of several sensors on a same chip.

In the next sections, we will present several nanophotonic biosensors on silicon-on-insulator: ring resonator based devices, slotted ring resonators and nanoplasmonic interferometers.

2. RINGS

SOI Microring Resonators

Biosensing with microcavities is considered a promising technique for label-free biosensing thanks to its high sensitivity and its potential for high throughput sensing with integrated cavity arrays.¹ The resonance wavelength shift resulting from a changing local refractive index when biomolecular interaction takes place in the vicinity of the cavity, is a quantitative measure for the number of binding events. In contrast to other integrated biosensor designs such as interferometers, light interacts multiple times with the assay. The long photon lifetime in the cavity results in sharp resonance peaks when converted to the frequency domain, so small peak shifts can be distinguished. Unlike the interferometer sensor response, the response signal of an optical cavity does not decrease with decreasing sensing area. A smaller cavity needs less molecules for entire coverage, while the signal remains high. For this reason we tend to refer to total mass coverage as a figure of merit for detection limit rather than surface coverage per area.

The microring resonators for this experiment are racetracks with 5 μm radius and 2 μm straight section for good coupling control. The waveguides are $220 \times 450 nm^2$ (figure 1A, 1B). The resonators have a quality (Q-) factor of 20,000 and a finesse of 240. The ultimate limit of detection is equal to the ratio of sensor resolution

Send correspondence to Peter Bienstman,
E-mail: Peter.Bienstman@UGent.be

and sensor sensitivity.² The sensitivity, the wavelength shift resulting from a molecular binding layer with a certain optical thickness, is dependent on the waveguide design and can be simulated using vectorial mode solver software. The designed waveguides have a sensitivity of $157 \text{ pm}/\text{nm}$ for a model bilayer with refractive index 1.45.³ The sensor resolution from the experiments here described is 2 pm . It is limited by the original signal quality, the fitting quality and the resonance wavelength stability in time. The original signal quality is dependent on Q-factor, extinction ratio and equipment noise. Although a high Q-factor is beneficial for the sensor's resolution, it sets high demands to the measurement equipment. By increasing the ring's radius, the Q-factor will increase. 20,000 is a value that holds a compromise between small surface area, small peak width and maximal extinction (critical coupling). The resonance wavelength stability is influenced by temperature and flow conditions. Care is taken to avoid drift on the signal. From the sensitivity and the resolution we can conclude that a layer with thickness of 12 fm can be detected. Using an approximated value of $1.33 \text{ g}/\text{cm}^3$ as molecular layer mass density,³ we can estimate a minimal detectable mass coverage of $17 \text{ pg}/\text{mm}^2$. As mentioned before, one of the benefits of using resonators rests on the fact that the response remains high for small surface area. With a surface area of only $21.84 \text{ }\mu\text{m}^2$ a minimal molecular mass of 0.37 fg could theoretically be detected.

Light is coupled from single mode fibers at 10° from the normal to the waveguides on the SOI chip through grating couplers.⁴ All measurements in paragraph 2 are performed with a superluminescent LED and an optical spectrum analyser. Spectra are stored every 3 seconds. After fitting all data to a Lorentzian, the resonance wavelength is plotted versus time. A flow cell is mounted on top of the chip and connected through tubings to a Harvard syringe

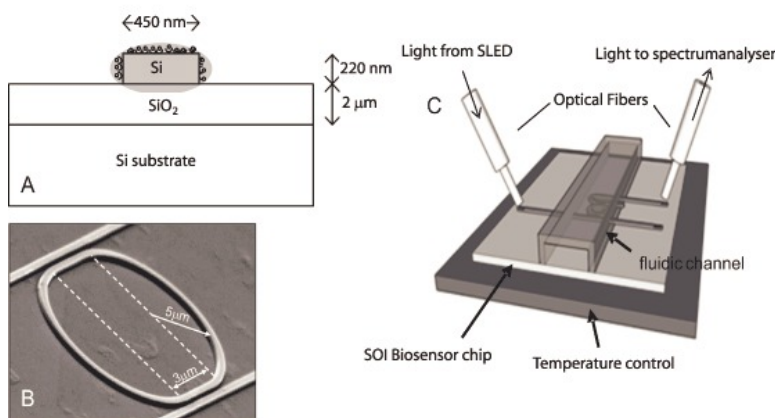


Figure 1: A) SOI waveguide for biosensing, B) SEM picture of a racetrack resonator, C) illustration of the measurement setup.

Poly(ethylene glycol) Layer for Highly Selective Biosensing

The quality of a biosensor critically depends on the interfacial layer, especially for detection in complex samples. The interfacial layer has to provide immobilization sites for the receptor molecules and at the same time effectively block non-specific interactions with the macromolecular components of the analyzed sample. It must be stable over a long time, must not affect the sensor's sensitivity and must not hinder transport of the biological compounds to the surface. Typically used coatings of silane reagents that can bear a wide range of functional groups for receptor molecule immobilization do not have sufficient resistance to non-specific adsorption. We improved this by attaching an ultra thin layer of hydrophilic poly(ethylene glycol) (PEG). The ability of PEG layers to reduce non-specific interaction is well documented.⁵ We introduce the PEG to the surface through a two steps process, the PEG layer is coupled to a silane layer bearing epoxide groups (figure 2). We examined two heterobifunctional PEG's with functional end-groups of very different reactivity towards epoxides. α -sulfanyl- ω -carboxy PEG (HS-PEG-COOH) and monoprotected diamino-PEG (H2N-PEG-NH-Boc) provide reactive carboxy and amino groups on the surface of the SOI microring respectively.

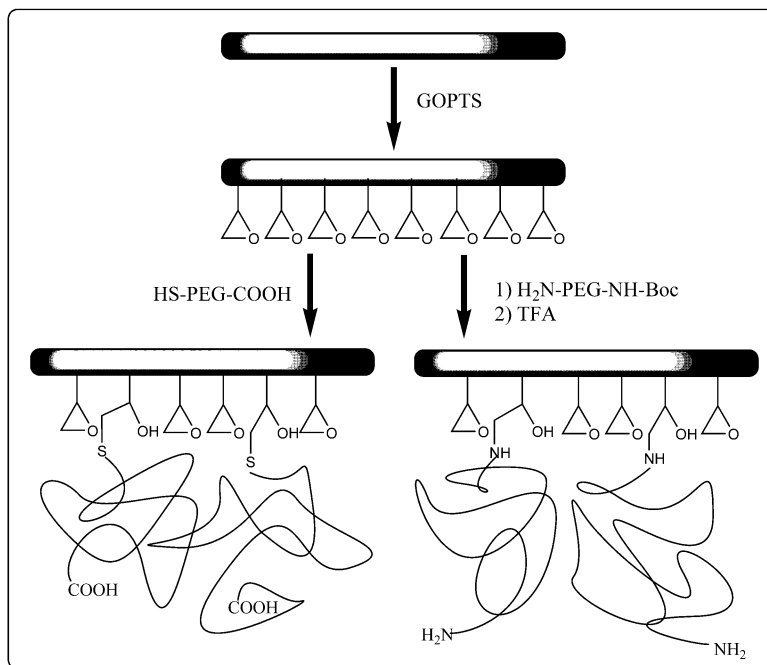


Figure 2: The chemical reaction for the coating of silicon surfaces with PEG layers (thicknesses are not too scale).

The functionalization procedure is characterized by ellipsometry, contact angle measurements and X-ray Photoelectron Spectroscopy. We obtain homogenous and thin surfaces. The HS-PEG-COOH and H₂N-PEG-NH-Boc layers have a thickness of respectively 2.3 and 2.5 nm and have a surface loading of respectively 99 pm/cm² carboxygroups and 97 pm/cm² aminogroups. The contact angles were reproducible (32° ± 1°), lower than the GOPTS-surface contact angle and comparable to literature values.

Specific and Non-Specific Interaction Results and Discussion

We used the high affinity avidin/biotin couple as a model to demonstrate repeatability and detection capabilities of the microring resonators. Bovine Serum Albumin (BSA), a protein with similar molecular weight to avidin, but with low affinity to biotin, has been used a model for non-specific interactions. Chips coated with H₂N-PEG-NH-Boc were deprotected first, biotinylated and placed in the optical setup. PBS was used as running buffer, the resonance wavelength of the ringresonator immersed in PBS was taken as reference signal. Figure 3A shows the response of the coated sensor to different avidin concentrations (17, 87.5 and 175 μg/ml) in contrast to the response to a high BSA concentration (1 mg/ml). Figure 3B shows that the response of 20 μg/ml BSA to a biotinylated microring resonator coated with APTES is only 5 times lower than its response to 20 μg/ml avidin.⁶ The low signal for high BSA concentrations when the sensor is coated with a PEG layer contrasts to the high signal for low BSA concentrations when the sensor is coated with an APTES layer. Applying a hydrophilic coating makes this proof-of-principle biosensor ready to be lined up in arrays and to be integrated in a microflow system for multiparameter biosensing on cheap disposable chips.

3. SLOTTED RINGS

3.1. Towards a higher accuracy

An important route towards an improvement of the sensitivity, and possibly of the accuracy and the detection limit, of this sensor, is to increase the interaction between light in the resonator waveguide and biomolecules attaching to the waveguide surface. When using a normal photonic wire, only the evanescent tail of the wire mode will interact with biomolecules (Figure 4, left). By etching a narrow slot in the middle of the waveguide,

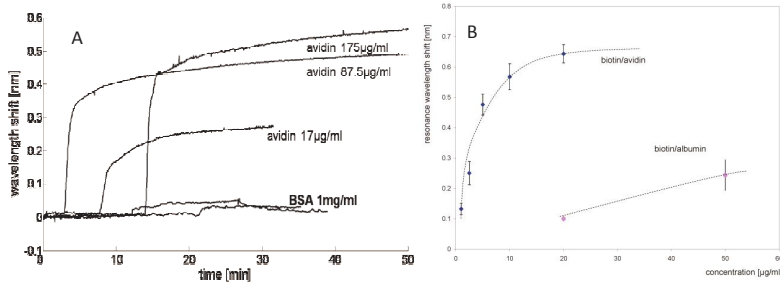


Figure 3: A) resonance wavelength shift versus time for the specific and non-specific interaction of a microring resonator coated with H2N-PEG-NH-Boc and biotinylated, B) resonance wavelength shift versus concentration for the specific and non-specific interaction of a microring resonator coated with APTES and biotinylated.

a vast fraction of the quasi-TE mode will be concentrated in that slot,⁷ so that more light is concentrated along the bio-activated surface of the slot waveguide (Figure 4, right). This will cause attached molecules to have a larger impact on the propagating light, so that the resonance wavelength shift of a racetrack resonator consisting of slot waveguides will be larger than that of a normal racetrack resonator. This concept already proved to be promising for biosensing.⁸

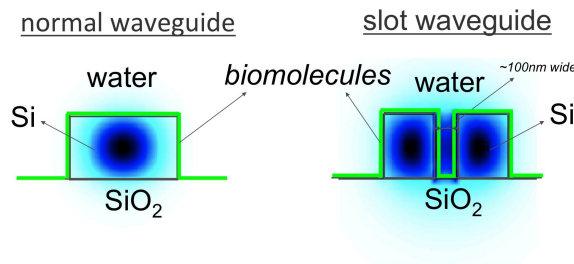


Figure 4: Comparison between the intensity profiles of the quasi-TE modes of a typical silicon photonic wire (450nm wide) and of a silicon slot waveguide (520nm wide with 100nm slot width). Both waveguides are 220nm high.

3.2. Waveguide design

Using an eigenmode expansion tool, the slot width S and strip width W of a silicon slot waveguide were optimized for biosensing. The height of the waveguide was kept constant at 220nm, as this was already fixed by our fabrication process. Surface sensing was simulated by a layer with refractive index 1.45 covering the whole waveguide (Figure 5, left).

As a function of slot width S and strip width W , the effective index of the waveguide was simulated once for 1nm biolayer thickness (model for initial surface chemistry) and once for 6nm biolayer thickness (model for saturated surface). Taking first order dispersion into account, the difference in effective index was used to calculate the expected resonance wavelength shift of the racetrack resonator applying this formula:

$$\Delta\lambda = \frac{(n_{eff,6nm} - n_{eff,1nm})\lambda_{res}}{n_g} \tag{1}$$

Here, λ_{res} is the initial resonance wavelength of the racetrack resonator and n_g is the group index of the slot waveguide at the resonance wavelength.

The graph in Figure 5 shows the calculated resonance wavelength shift as a function of S and W . In this range of the parameters, the smaller the slot width S becomes, the higher the sensitivity will be, and for each value of S , the optimal value for W can be read from the graph.

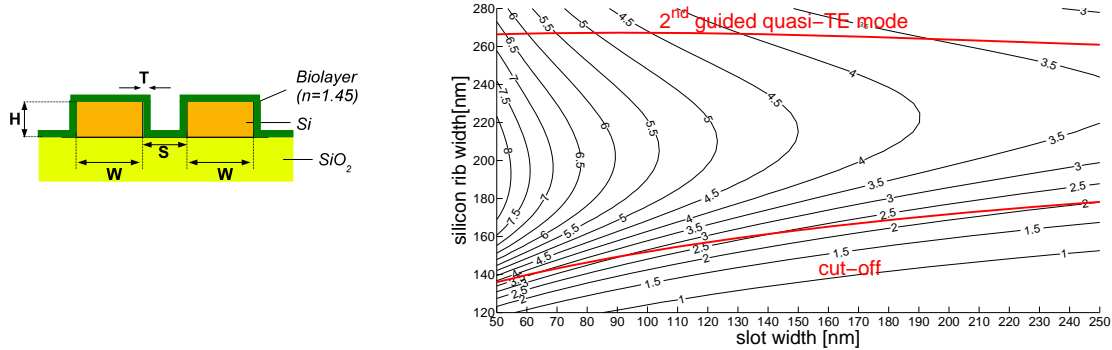


Figure 5: Left: Simulated cross section of the racetrack slot waveguide. A biolayer is used to model the surface chemistry and attaching of biomolecules to the waveguide surface. Right: Simulated shift of the slotted racetrack resonator as a function of the slot width and rib width of the waveguide, when the sensor is saturated with biomolecules (full coverage of the waveguides). The single mode regime for the quasi-TE polarization is indicated.

3.3. Fabrication

Slotted racetrack resonators with $5\mu m$ radius and $3\mu m$ straight coupling sections were fabricated with deep-UV lithography.⁹ Figure 6 shows scanning electron microscope images of our slotted racetrack resonator with 100nm slot width.

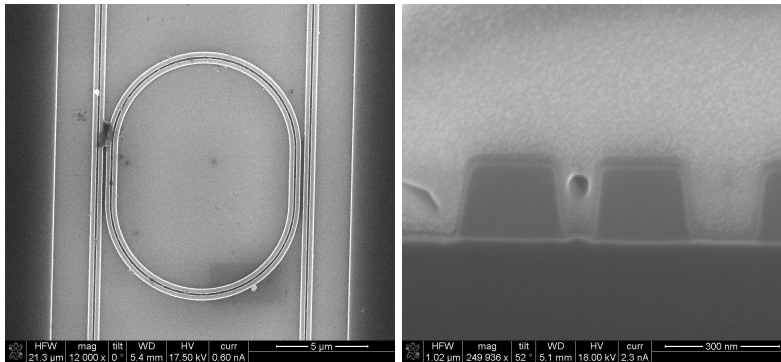


Figure 6: Left: scanning electron microscope image of the slotted racetrack resonator with $5\mu m$ radius, fabricated with deep-UV lithography. Right: cross section of the silicon slot waveguide with 100nm slot width (measured at half height).

3.4. Bulk refractive index sensing

The bulk sensitivity of this slotted racetrack resonator was measured by flowing watery NaCl-solutions with different concentrations over the sensor. A flow cell with closed channel was used to avoid evaporation and no surface chemistry was applied to the sensor surface for this experiment. The left graph in Figure 7 shows the shift of a resonance dip in the pass spectrum of the slotted racetrack, when different salt concentrations are flown over. Lorentzian fitting was used to determine the resonance wavelength. This resonator has a quality factor of 420.

The right graph in Figure 7 shows the linear shift of the resonance wavelength as a function of the top cladding index, where the refractive index of the salt solutions was determined¹⁰ at a wavelength of 1550nm. The bulk

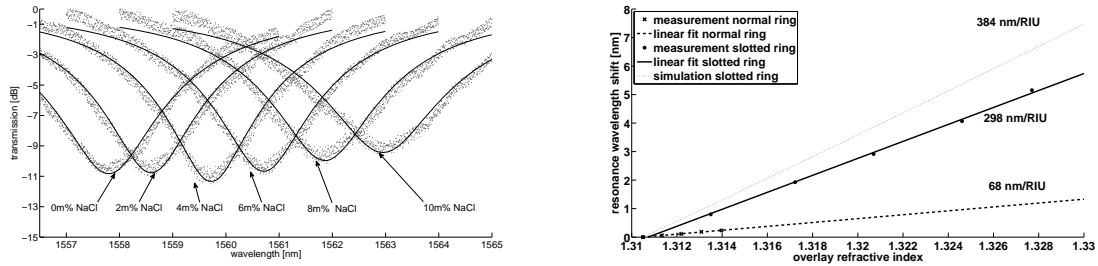


Figure 7: Left: Resonance dip in the pass spectrum of the slotted racetrack resonator for different salt concentrations. Right: Comparison between the experimental resonance wavelength shift of a normal racetrack and the theoretical and experimental resonance wavelength shift of a slotted racetrack as a function of the overlay refractive index. Experimental data¹⁰ was used to determine the refractive index of the salt concentrations.

sensitivity of the slotted racetrack resonator with 100nm slot region is 298nm/RIU as compared to 68nm/RIU for normal racetracks. Using an eigenmode expansion tool, the effective index change of a slot waveguide with the same dimensions as in Figure 6 was simulated for changing top cladding index. Based on this, a theoretical bulk sensitivity of 384nm/RIU was calculated, taking first order dispersion into account.

4. SURFACE PLASMON INTERFEROMETER

Introduction

Another potentially interesting route toward label-free biosensing is the combination of Surface Plasmon interrogation techniques and Silicon-on-Insulator as a host substrate.^{11,12}

Surface Plasmon Polariton modes are very sensitive to refractive index changes due to the very high evanescent fields near the surface on which they propagate. Besides this physical advantage, there is also a chemical advantage to using thin gold layers in biosensors, gold boasts the advantage that it is a bio-compatible material and a very mature thiol-chemistry can be used for the functionalisation of this layer.

However, the integration of surface-plasmon waveguide structures in Silicon-on-Insulator is not that straightforward. A high index contrast material system puts fundamental limits to the resonant excitation of surface plasmons at a gold-water surface. Phase-matching of guided waveguide modes with surface plasmon modes can be obtained, but only for modes with an effective index that is much lower than the refractive index of the waveguide. Moreover, the operating spectral range of such a device will be limited and set by the conditions for phase-matching, as is the case in conventional SPR waveguide sensors.

The principle of a Surface Plasmon Interferometer is based on the interference of two decoupled Surface Plasmon modes propagating on either side of a thin gold layer embedded into a Silicon waveguide. The high degree of asymmetry associated with the gold layer (top interface $n \propto 1.33$, bottom interface $n \propto 3.45$) assures that the surface plasmon modes associated with the upper and lower of the metal-dielectric interfaces will be decoupled. Excitation is done by end-fire coupling from a regular SOI waveguide. The phase of the top surface plasmon mode is influenced by the refractive index of the environment, while the phase of the bottom surface plasmon mode is insensitive to refractive index changes. Upon recombining, depending on the relative phase of both surface plasmon modes, the dielectric TM waveguide mode will experience destructive or constructive interference.¹¹

Theoretical results predict that this device would be capable of detecting very small refractive index changes (10^{-6} RIU) for a device which has a physical footprint of only $100 \mu m^2$.

5. FABRICATION

The sample used for experimental verification consists of a Silicon substrate, $2 \mu m$ of HDP-Silicon dioxide and 220 nm of a-Si, deposited using a PECVD process with Silane and He gases.¹³ The devices were fabricated

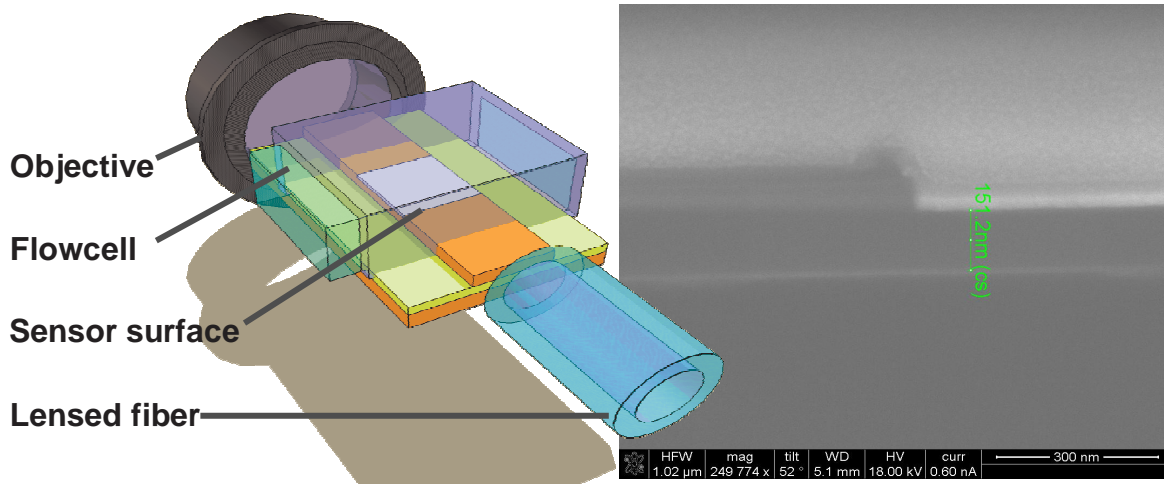


Figure 8: Left: Schematic representation of the Surface Plasmon Interferometer, the flowcell and the measurement setup, right: FIB cross-section of the fabricated device.

using Deep-UV Lithography in IMEC. To ensure that we have a working prototype, several different designs were processed simultaneously. The lengths of the gold embedded strip varies from 4 to 10 μm , in steps of 1 μm , Si-waveguides used had widths of 10, 3 and 0.550 μm . Etch depth of the sensor region in the Si was 70 nm , the Au layer was deposited using thermal evaporation and has a thickness of 37 nm . A protective layer of BCB (CYCLOTENE XU35133) was used for this chip to prevent the flowcell from damaging the Si-waveguides. Although the parameters mentioned here are certainly not the ideal parameters for sensing applications, in the sense that the wavelength shift per refractive index unit should be as large as possible, they were chosen merely for the purpose of obtaining proof-of-principle. An FIB cross-section of the fabricated device can be seen in on the right side of figure 8.

6. MEASUREMENT RESULTS

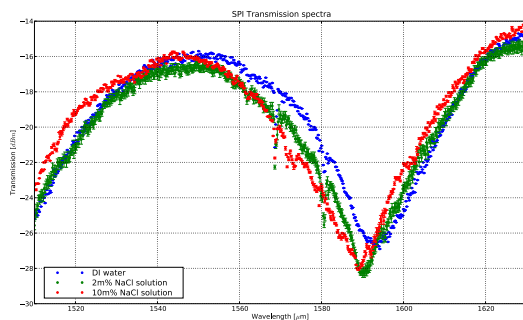


Figure 9: Measured transmission spectra for different NaCl concentrations

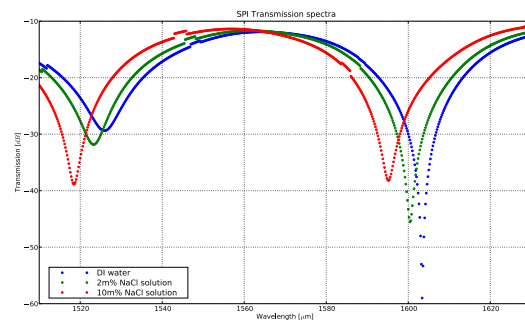


Figure 10: Simulated transmission spectra for different NaCl concentrations

Light from a single mode fiber was coupled into the sample using a lensed fiber, outcoupling occurs through an objective. Measurements have been performed using a tunable laser (output power 5 mW) and power detector, to ensure that only TM polarized light is measured a polarizer has been used in front of the detector.

The measurement data presented here was obtained for a sensor with length 8 μm . DI-water, a solution of 2 $\text{m}\%$ of NaCl and a solution of 10 $\text{m}\%$ of NaCl were flown over the sensor surface consecutively. Absolute mean deviation error bars represent the fact that for each length, several spectra were measured with an interval

of 10 *min* to ensure that we were measuring the steady-state response rather than some transient effect. For comparison, theoretical results are also depicted on the right. Theoretical curves were calculated using CAMFR, an in-house developed eigenmode expansion tool.¹⁴

From the measurement results one can see that this device is indeed capable of bulk refractive index sensing. The measured spectra show a qualitative agreement between experiment and theory. By using the centroid method, the decision level being the average transmission, one can easily determine the wavelength of minimal transmission. The wavelength of minimal transmission versus the refractive index of the analyte flown over the sensor surface is depicted in figure 11. Using this data we can estimate the general sensitivity of this device to be $234.4 \text{ nm}/RIU$. Theoretically one would expect a sensitivity of $358 \text{ nm}/RIU$.

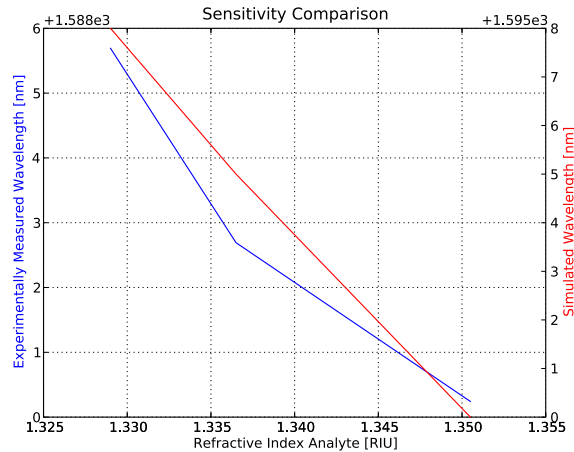


Figure 11: Comparison of the experimentally measured and the simulated sensitivity

7. CONCLUSION

We presented several nanophotonic biosensors on silicon-on-insulator: ring resonator based devices, slotted ring resonators to increase the interaction between light and the sample, and finally devices based on nanoplasmonic interferometers. We also presented optimized chemistry to limit non-specific binding.

ACKNOWLEDGMENTS

Parts of this work were performed within the context of the Belgian IAP project Photonics@BE.

REFERENCES

1. F. Vollmer and S. Arnold, “Whispering-gallery-mode biosensing: label-free detection down to single molecules,” *Nature Methods* **5**(7), pp. 591–506, 2008.
2. I. White and X. Fan, “On the performance quantification of resonant refractive index sensors,” *Optics Express* **16**(2), pp. 1020–1028, 2008.
3. J. Vörös, “The Density and Refractive Index of Adsorbing Protein Layers,” *Biophysical Journal* **87**, pp. 553–561, 2004.
4. W. Bogaerts, R. Baets, P. Dumon, V. Wiaux, S. Beckx, T. D. B. Luyssaert, J. Van Campenhout, P. Bienstman, and D. Van Thourhout, “Nanophotonics Waveguides in Silicon-on-Insulator Fabricated with CMOS Technology,” *Journal of Lightwave Technology* **23**(1), pp. 401–412, 2005.
5. L. Andruzzi, W. Senaratne, A. Hexemer, E. Sheets, B. Ilic, E. Kramer, B. Baird, and C. Ober, “Oligo(ethylene glycol) Containing Polymer Brushes as Bioselective Surfaces,” *Langmuir* **21**, pp. 2495–2504, 2005.

6. K. De Vos, I. Bartolozzi, E. Schacht, P. Bienstman, and R. Baets, "Silicon-on-Insulator microring resonator for sensitive and label-free biosensing," *Optics Express* **15**, pp. 710–715, 2007.
7. V. R. Almeida, Q. Xu, C. A. Barrios, and M. Lipson, "Guiding and confining light in void nanostructure," *Optics Letters* **29**, pp. 1209–1211, june 2004.
8. C. A. Barrios, M. J. Banuls, V. Gonzalez-Pedro, K. B. Gylfason, B. Sanchez, A. Griol, A. Maquieira, H. Sohlstrom, M. Holgado, and R. Casquel, "Label-free optical biosensing with slot-waveguides," *Optics Letters* **33**, pp. 708–710, APR 1 2008.
9. www.epixfab.eu.
10. H. Su and X. G. Huang, "Fresnel-reflection-based fiber sensor for on-line measurement of solute concentration in solutions," *Sensors and Actuators B-Chemical* **126**, pp. 579–582, OCT 1 2007.
11. P. Debackere, S. Scheerlinck, P. Bienstman, and R. Baets, "Surface Plasmon Interferometer ," *Optics Express* **14**(16), pp. 7062–7072, 2007.
12. R. Baets, D. Taillaert, W. Bogaerts, P. Dumon, K. De Vos, P. Debackere, S. Scheerlinck, and D. Van Thourhout, "Silicon Nanophotonics and its Applications in Sensing ," *proceedings CLEO* , pp. 1221–1222, 2007.
13. S. Selvaraja, E. Sleenckx, W. Bogaerts, M. Schaekers, P. Dumon, D. Van Thourhout, and R. Baets, "Low loss amorphous silicon photonic wire and ring resonator fabricated by CMOS process ," *proceedings of ECOC* , 2007.
14. P. Bienstman and R. Baets, "Optical Modeling of Photonic Crystals and VCSELs using Eigenmode Expansion and Perfectly Matched Layers ," *Opt. Quantum Electron* **33**(4–5), pp. 327–341, 2001.